Research Article Vol. 33, No. 22 / 3 Nov 2025 / Optics Express 46599
Optics EXPRESS

Automatic and adaptive optical wireless power transmission for IoT with dual mode of day and night charging

MINGZHI ZHAO AND TOMOYUKI MIYAMOTO*

Laboratory for Future Interdisciplinary Research of Science and Technology (FIRST), Institute of Science Tokyo, R2-39, 4259 Nagatsuta, Yokohama 226-8503, Japan
tmiyamot@pi.titech.ac.jp

Abstract: Optical wireless power transfer (OWPT) has emerged as a promising solution for efficient energy delivery. This study proposes an adaptive OWPT system capable of dynamically adjusting the beam spot size according to the distance and size of the optical receiver, enabling efficient energy concentration at distances of up to 5 m. Furthermore, the system incorporates optimized hybrid image processing techniques to enhance the localization accuracy of both the irradiation spot and optical receivers under varying lighting conditions, including both illuminated and unlit environments. Experimental results confirm that the system can stably power multiple receivers while seamlessly switching between bright and dark modes without interruption. The system consistently delivers reliable power across diverse scenarios, validating its adaptability and potential for scalable wireless power delivery in dynamic environments.

1. Introduction

The rapid expansion of Internet of Things (IoT) has increased the demand for efficient and flexible power solutions. Both traditional methods of batteries and cable connections have limitations. Batteries provide low functionality due to limited provided power and require frequent replacement or charging, while cable connections restrict device placement and mobility. To overcome these limitations, far-field wireless power transmission (WPT) utilizing radio frequency or microwave has emerged as a viable alternative [1–4]. However, they require large antenna arrays for efficient transmission or suffer from low utilization efficiency due to wavelength-dependent spatial size. They are also susceptible to electromagnetic interference (EMI) [5]. Given these limitations, optical wireless power transmission (OWPT) emerges as an alternative by leveraging high-frequency optical waves for efficient energy transmission. OWPT enables more focused energy with a more compact transmitter design. Additionally, OWPT can integrate with optical wireless communication for high-performance simultaneous wireless information and power transmission (SWIPT) [6–9]. These advantages make it a promising solution for long-distance transmission, high directionality, and no EMI operation [10]. Thus, OWPT combines the advantages of both flexibility and reliability.

In recent years, OWPT research has developed rapidly towards more practical and application-oriented solutions. In 2016, John Fakidis et al. demonstrated an indoor OWPT system using red laser diodes to charge small cells at night [11]. In 2021, Qingwen Liu et al. presented resonance-based OWPT system, achieving over 0.6 W of electrical power for remote and mobile smartphone charging [12]. Nadeem Javed et al. extended OWPT transmission to 30 m in free space using an optimized Erbium-doped fiber amplifier (EDFA) [13]. From 2024, Duchang Heo et al. demonstrated the 808 nm laser diodes based OWPT for powering multiple acoustic emission sensors [14]. Jinsong Kang et al. presented resonance-based OWPT for high-precision beam alignment [15,16]. Mahiro Kawakami et al. analyzed OWPT infrastructure layout for electric vehicles [17]. Most OWPT research has focused on laser-based systems. However, when applied

#574553 https://doi.org/10.1364/OE.574553
Journal © 2025 Received 28 Jul 2025; revised 23 Sep 2025; accepted 13 Oct 2025; published 24 Oct 2025

Optics EXPRESS

to IoT scenarios, such systems must comply with strict Maximum Permissible Exposure (MPE) regulations, such as IEC 60825, to prevent potential eye or skin hazards [18]. This requirement makes laser-based OWPT unsuitable for indoor environments, especially in confined spaces where humans or animals may be present.

For indoor IoT scenarios, we propose a light-emitting diode (LED) based OWPT approach that ensures both safety and reliable power transmission [19,20]. Compared to laser-OWPT, LEDs have lower power density, making it easier to design for complying with safety regulations [21]. Second, the broader divergence of LED provides flexible beam coverage, enhancing the tolerance for precise alignment between the transmitter and receiver [22]. Third, LEDs have long lifespan and low temperature sensitivity with low cost, allowing seamless integration into existing lighting infrastructure as compact modules [23,24]. These features make LED-OWPT particularly suitable for indoor and living things-inhabited environments, including smart homes, factories, and farms.

However, LED-OWPT still faces several challenges. First, energy transfer efficiency decreases significantly over long distances, limiting practical power output [25]. Second, existing systems lack the capability to power multiple targets automatically and simultaneously. Furthermore, conventional detections in LED-OWPT are highly sensitive to ambient lighting conditions, affecting its reliability in varying illumination environments [26]. Addressing these challenges is crucial for advancing LED-based OWPT toward real-world IoT applications.

In this paper, we propose an LED-OWPT system featuring an adaptive optical design for efficient long-distance power transmission and an optimized detection framework for reliable beam aiming. The proposed system enables precise and uninterrupted automatic power delivery to multiple terminals, even under varying lighting conditions. Section 2 details the optical system design and beam aiming mechanism. Section 3 presents the enhanced detection algorithm for irradiation spots and receivers, along with the methodology for ensuring stable power transmission under varying lighting conditions. Section 4 presents experimental results and performance evaluation. Section 5 discusses the challenges for future development, and Section 6 concludes this research.

2. System design and simulation

2.1. Adaptive optics system for long distance transmission

In our previous studies, we optimized a collimation-focus lens-based LED-OWPT system for 1 m distance transmission, where a $50 \times 50\,\mathrm{mm}^2$ optical receiver matched the focused irradiation spot. However, beyond 1 m, the spot size increased significantly, leading to severe power attenuation, even over 90% energy loss at 3 m [25, 27]. Thus, the core design of long-distance OWPT is to maintain a small irradiation spot during transmission.

To overcome the limitations of transmission distance and power attenuation, we propose an adaptive lens system with a double-layer lens configuration consisting of one tunable focal length lens (Lens 1) and an imaging lens (Lens 2). The positions of the lenses on the optical axis are fixed, while the focal length of one lens is adjusted to control the irradiation spot size. Compared to the high-performance beam shaping method that relies on physically shifting lens positions on the optical axis [28], the proposed approach offers faster response and a more compact form factor.

Lens 1 functions as a converging lens and is positioned near the LED to reduce its large beam divergence. By dynamically adjusting its focal length, it ensures that the irradiation spot remains well-matched to the receiver size, thereby maintaining a high energy density and minimizing power loss over long distances. In addition, the tunability of Lens 1 allows for flexible control of the entrance pupil size and the injection angle into Lens 2. This enables dynamic regulation of magnification, which is the ratio of image height to object height. According to Gaussian optics,

Optics EXPRESS

the magnification M in such a double-layer lens system can be derived as:

$$\mathrm{M} = \frac{l_2' f_1}{\mathrm{d}(l_1 - f_1) - f_1 l_1} \tag{1}$$

Here, f_1 denote the focal lengths of Lens 1, l_1 is the object distance (from the light source to Lens 1), l_2' is the imaging distance (from Lens 2 to the image plane), and d is the physical distance between Lens 1 and Lens 2. The parameters in Eq. (1) are illustrated in Fig. 1 for clarity. It is obverse that, the magnification M is directly proportional to the imaging distance l_2'. To achieve a reduced spot size (i.e., smaller magnification), it should decrease the focal length f_1 of Lens 1 and increase the distance d between the two lenses.

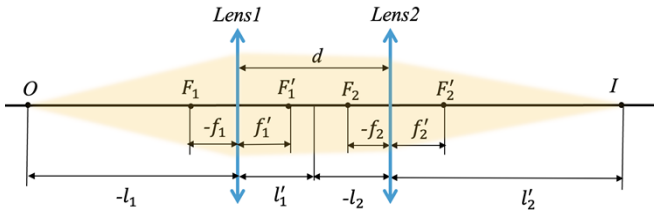

Fig. 1. Configuration of the double-lens system.

In practical implementation, however, a large lens distance d can cause the light beam to extend beyond the aperture of Lens 2. This leads to power loss and degrades the transmission efficiency. In addition, the transmitter-side length becomes unnecessarily extended, increasing the overall dimensions of the system. Therefore, we proposed the optical system parameters based on simulations that balance magnification control with beam confinement. Figure 2 shows the lens configuration. Lens 1 is implemented as a tunable-focus element that supports both short- and long-distance transmission within a single optical system. As an investigation of the boundary conditions, when Lens 1 is set to f = + 10 mm, the system is optimized for short-distance transmission, resulted a focused spot at 0.5 m imaging distance. In contrast, when Lens 1 is tuned to f = –20 mm, the system enables long-distance transmission with reduced spot divergence of a focused spot at around 10 m. Lens 2 is a fixed-focus lens with a focal length of 1000 mm and a diameter aperture of 100 mm. The optimal object distance is l_1=15 mm, and the lens separation distance is d = 70 mm. This configuration enables a compact and adaptive optical system for spot size control while maintaining high power transmission performance over longer distances.

2.2. *Dual-axis reflector based aiming system*

Beam aiming systems can be categorized into mechanical and non-mechanical methods. Beam forming based non-mechanical approach offers limited steering angles and restrict the power charging range. On the other hand, Mechanical approaches provide larger steering angle, divided into direct transmitter rotation and indirect reflection. The direct transmitter rotation method is prone to optical axis misalignment during high-speed rotation of components. Even a slight deviation of 1 mm can result in significant targeting errors [25,29]. To overcome these challenges, we design a dual-axis reflector-based beam aiming system. One reflector positioned after the imaging lens, rotates along two axes for precise beam steering on the xz-plane along y-axis. The simulated transmitter side is shown as Fig. 3.

The beam aiming system builds on the structural design from our previous auto-OWPT research. It employs two series-connected stepping motors, allowing independent rotation along both the horizontal and vertical axes. Two motors operate via an Arduino-based pulse width modulation

Optics EXPRESS

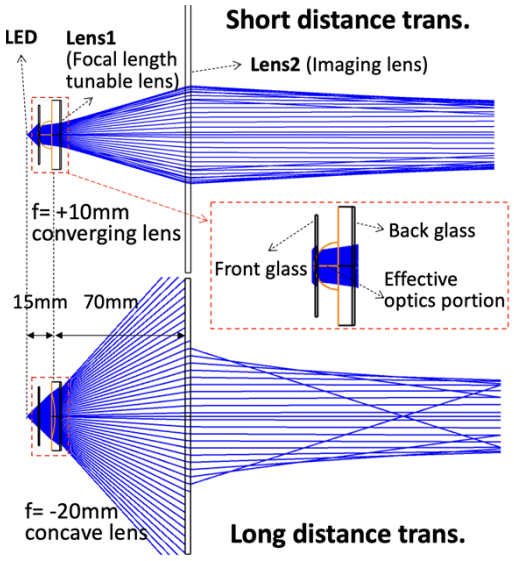

Fig. 2. Schematic of the adaptive optical system. Lens 1 applies as a tunable-focus lens (for example, f = 10 mm for ~0.5 m short-range focusing, f = –20 mm for ~10 m long-range focusing). Lens 2 (f = 1000 mm, aperture = 100 mm) further collimates the beam as an imaging lens.

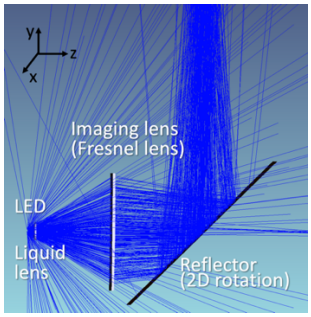

Fig. 3. Simulated configuration of automatic and adaptive LED-OWPT.

(PWM) control system, where the Arduino functions as a server, receiving real-time positioning instructions based on PC image detection results.

To ensure precise beam alignment, both the photovoltaic (PV) receiver and irradiation spot positions must be identified. For this purpose, an Intel RealSense D435 depth camera is integrated, featuring one RGB sensor and two infrared (IR) sensors. The RGB camera detects the PV position, while the IR camera identifies the irradiation spot. Based on the detected PV position, the system adjusts the reflector's orientation to adjust the irradiation spot position. This process continues until the position difference between the PV and the spot reaches zero, ensuring precise alignment regardless of target movement or distance changes. In addition, spot adjustment dynamically modifies the beam size based on the detected PV dimensions, ensuring that the spot size matches the corresponding target size. The total system design concept is shown as Fig. 4.

Optics EXPRESS

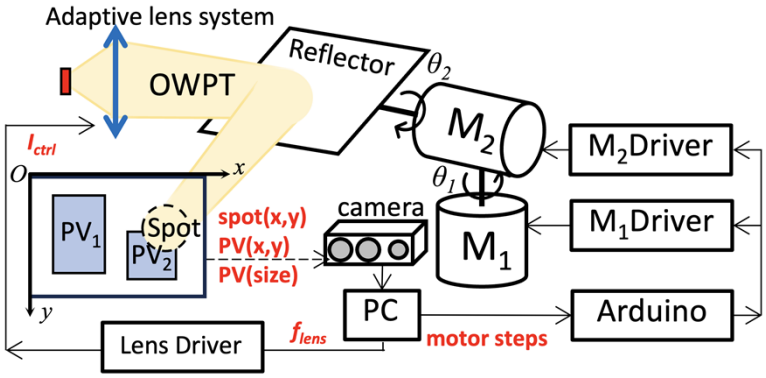

Fig. 4. Concept of automatic and adaptive OWPT system.

3. Automatic power supply in varying lighting conditions

3.1. Improved PV detection algorithm

In previous approaches to PV detection, we applied RGB camera to identify PV cells within illuminated environments [26]. However, in low-light or no-light environments, the lack of visible light rendered the RGB based algorithm unable to detect the PV. To achieve precise beam aiming and ensure continuous operation under both illuminated and dark conditions, we optimize the image processing methodology by implementing a retroreflector (RF) based detection approach. RF is for reflecting incident light back toward its source over a wide range of incidence angles. This is typically achieved using structures such as corner cube prisms or high-index microbeads embedded in a reflective layer. When light is incident on a retroreflector, it undergoes at least two internal reflections, ensuring the reflected beam travels nearly parallel to the incoming beam. Leveraging this property, the proposed PV detection can work under low-light or no-light conditions. Figure 5 shows the mechanism of the PV detection in environments with and without illumination. A commercial depth camera capturing RGB and IR images, also has an IR projector that generates a pattern of IR dots for enhancing depth perception in low texture scenes and auxiliary depth calculation. This IR dot pattern is also feasible for optimized PV detection in low-light settings.

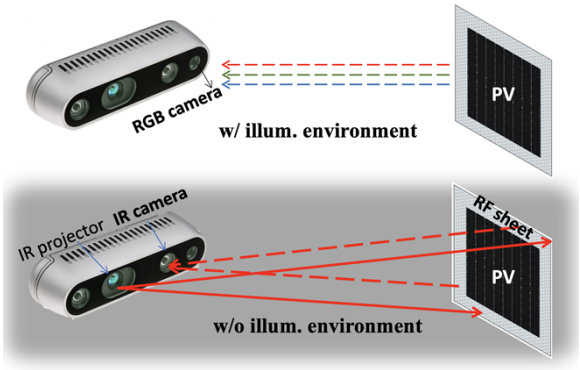

Fig. 5. PV detection in environments with and without illumination. Under illumination, PV is detected via the RGB sensor. In the absence of illumination, the IR projector from the depth camera emits IR dots, which are reflected by the retroreflector and captured by the IR sensor.

Optics EXPRESS

As shown in Fig. 6(a), the camera projects these IR dots to the objects. We attach retroreflector sheets around the PV cells. When these IR dots irradiated on the retroreflector sheet surrounding PV cell, they are reflected to the camera's IR sensor, creating a distinctive outline of the PV cells, as shown in Fig. 6(b). This IR-based detection is entirely unaffected by the external light conditions, as the depth camera's IR source itself generates the necessary features for detection.

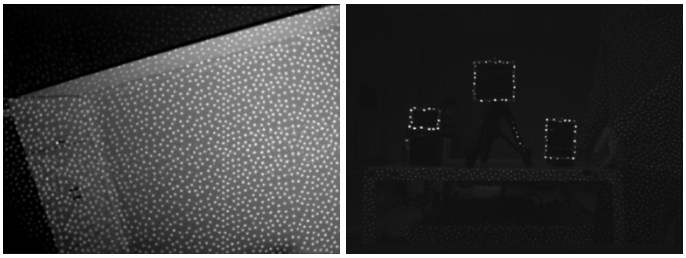

(a) (b)

Fig. 6. IR image of (a) IR dots from the depth camera IR projector; (b) IR dots on the retroreflectors of PV, even in the no-light environment, it can show the PV target outlines.

To boost the detection accuracy of the auto-OWPT system, we applied a convolutional neural network (CNN) based on the Single Shot MultiBox Detector (SSD) algorithm [30]. The model is built on the VGG16 backbone and includes 11 convolutional layers that output six feature maps of varying resolutions. Each of these maps is paired with a set of anchor boxes used to locate and classify objects. By setting the smallest anchor box scale to 11, the model becomes more effective at spotting small objects. Compared with the You Only Look Once (YOLO) algorithm [31], SSD offers better results for small object detection because it analyzes features across multi-scale feature maps, allowing small pixel size object to be captured.

Figure 7 shows the SSD network training process. We prepared and labeled a dataset of 3000 RGB images of PVs in the bright environments, and 1,000 IR images showing the IR-dotted PV outlines. These images were used to train the SSD network and achieved the mean average precision (mAP) of 0.87. The training results tend to be convergent after 300 epochs.

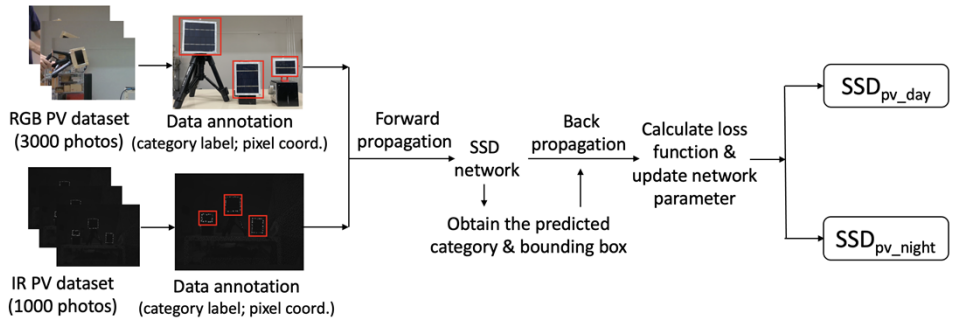

Fig. 7. The optimized SSD network is trained separately to detect PVs under illuminated (SSD_{PV_day}) and unlit (SSD_{PV_night}) environmental conditions.

3.2. *Optimized spot detection*

Previous study of SSD based IR spot detection has shown consistent and accurate results for large irradiation spot detection [26]. However, in scenarios involving smaller PV cells, the detected irradiation spot range was misinterpreted and located on the background wall instead of the PV

Optics EXPRESS

surface. This issue becomes more pronounced when using an LED array system for long-distance light transmission, as the irradiation spot on the background can often appear significantly larger than the actual PV cell area. This causes the center misalignment issue. To overcome this limitation, we develop an approach also based on the retroreflector that detects the irradiation spot range directly on the PV cell, thereby achieving higher detection precision for smaller target areas.

For this improved spot detection, we utilize the IR images captured by the depth camera, processing them through OpenCV to isolate the spot area with minimal interference. An essential step involves adjusting the camera exposure to reduce overexposure and eliminate excessive brightness that can obscure accurate detection. The default IR camera exposure setting of 8600 is reduced to 1000, limiting brightness noise in the captured IR images.

In the image processing pipeline, each pixel $G(i,j)$ in the grayscale, single-channel IR image is compared to a brightness threshold, set at half the intensity of the brightest pixel in the image G_{max}. Pixels with brightness values exceeding this threshold are converted to white, while others are set to black, producing a binarized image. This is represented as:

$$B(i,j) = \begin{cases} 255, & G(i,j) \geq 0.5 \times G_{max} \\ 0, & G(i,j) < 0.5 \times G_{max} \end{cases} \tag{2}$$

Following binarization, we apply morphological erosion to the resulting image, removing small, isolated areas of noise that could otherwise interfere with accurate spot detection. This operation, represented as $E(i,j)$, minimizes each pixel value within a specified neighborhood:

$$E(i,j) = \min_{i',j':k} B(i+i', j+j') \tag{3}$$

where $k(i',j') \neq 0$. The erosion step effectively eliminates minor white specks that do not correspond to meaningful spot information.

Subsequently, we filter out white regions that are either too small or excessively large, further refining the image to isolate only the irradiation spot. This filtering step is defined as:

$$F(i,j) = \begin{cases} 255, & 50 \leq \sum (i,j)_{E=255} \leq 1000 \\ 0, & \sum (i,j)_{E=255} > 50 \ or < 1000 \end{cases} \tag{4}$$

Figure 8 shows the outcomes of each processing step, resulting in a small, well-defined irradiation spot that is unaffected by external disturbances.

The performance of the proposed spot detection for irradiation spot on PV is demonstrated in Fig. 9. By highlighting only the high-brightness reflections from the retroreflector, the system isolates the irradiation spot on the PV surface, disregarding the spot on the background and focusing exclusively on the PV cell itself, even in low or no-light conditions. This approach confirms the system's capability to accurately identify the irradiation spot on the PV, mitigating interference from surrounding objects or background, and thereby enhancing detection accuracy and reliability.

3.3. Function of day and night auto-OWPT

To ensure continuous and precise power delivery, we design the system for seamless day-and-night operation, enabling reliable PV detection and beam alignment regardless of ambient light levels. Figure 10 shows the flowchart of the auto-OWPT system. The system begins by streaming both RGB and IR frames captured by a depth camera. These frames provide the foundation for determining whether the environment is illuminated (day mode) or unlit (night mode), which directly influences the method of PV detection.

Optics EXPRESS

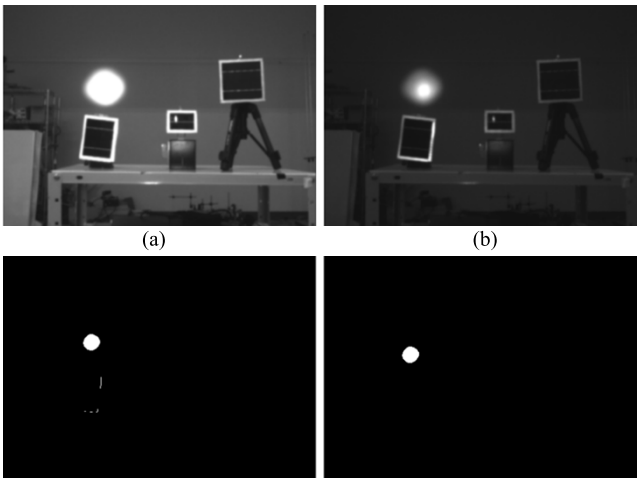

Fig. 8. Image processing pipeline for spot detection: (a) Original IR image with default exposure. (b) Decrease exposure to 1000. (c) Binarize the image according to threshold. (d) Erode and filter the small white noise.

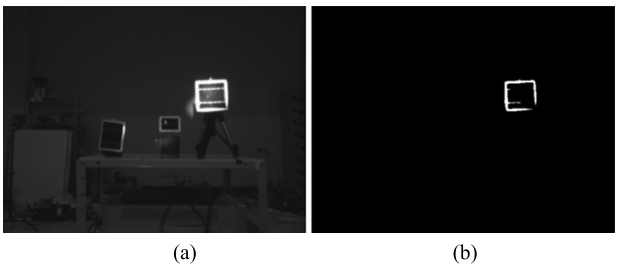

Fig. 9. (a) Irradiation spot on PV shown in IR image with low exposure; (b) After image processing, the white portion is regarded as spot range in the binary image.

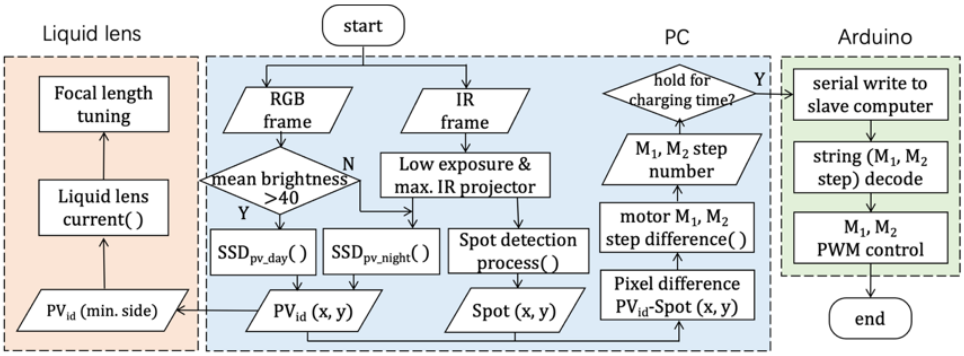

Fig. 10. Flowchart of the automatic and adaptive OWPT.

Optics EXPRESS

First, the system evaluates ambient brightness using the RGB sensor of depth camera, determining "day mode" if the mean brightness exceeds 40 of 255. In this mode, a pre-trained SSD neural network detects PV cells using RGB images. If brightness is less than 40, the system switches to "night mode," relying on IR images to detect PVs based on the IR reflection properties of the retroreflective sheet. This dual-mode approach ensures reliable PV detection cross varying lighting conditions. For multiple PV receivers, the system assigns each detected PV a unique sequence ID and records its pixel coordinates. Simultaneously, the system processes IR frames to detect the irradiation spot, identifying its center coordinates on the PV.

Then the system calculates the pixel difference between the PV center and the spot center for aligning the power beam on the targeted PV. This alignment process converts the pixel difference into step control instructions for two stepping motors. The instructions from PC are sent to the Arduino microcontroller, which decodes them and controls the motors via motor drivers and PWM. For multiple PVs, the system selectively targets specific receivers and maintains focus for a set charging duration.

Additionally, a focal length tunable liquid lens dynamically adjusts the spot size. There are two possible approaches to controlling the focal length of the liquid lens. The first method involves using depth data from the depth camera to adjust the focal length. However, since the IR OWPT spot is irradiated onto the target PV and the depth camera relies on an IR stereo vision system, it cannot obtain accurate and stable depth information effected by the high-density power beam. To overcome this limitation, we propose an alternative approach of relying on the detected PV's bounding box. Specifically, the system extracts the pixel value of the bounding box shortest side length as a reference and adjusts the focal length of the liquid lens, ensuring the irradiation spot size matches the target PV. This adaptive control enhances the longer distance transmission efficiency by dynamically aligning the spot size with PVs of varying dimensions.

3.4. Stabilizing PV detection in fixed system

While the auto-OWPT system achieves high accuracy in tracking and irradiating PV cells, maintaining consistent detection of small PV targets remains a challenge. Due to the neural network's optimization for small-object recognition, occasional detection failures occur in successive frames. These intermittent losses can disrupt continuous power delivery, which is critical for stable PV targeting in fixed applications. In mobile systems, tracking interruptions are mitigated by the prediction algorithm, which predicts PV positions based on updated location and velocity parameters, compensating for temporary detection failures [26]. However, this approach is ineffective in fixed systems, where PV cells remain stationary. Here, trajectory prediction methods do not apply, as there is no continuous movement to extrapolate.

To address this limitation, we propose a detection stabilization strategy based on data retention and position verification, ensuring consistent PV identification even when brief detection losses occur. As illustrated in Fig. 11(a), the system stores detected PV coordinates in a data array and applies positional thresholds to filter out temporary detection failures. Upon initial detection, each PV is assigned a unique identifier (PV_{id}), and an associated data array is created to record its center coordinates, denoted as $PV(x, y)$. For example, if five PVs are detected, the system generates five data arrays, each linked to a unique PV_{id}, continuously updating the respective PV center coordinates. This method enhances detection stability, ensuring reliable PV recognition and uninterrupted power transmission.

In scenarios where a PV disappears temporarily from the detection output by minor misrecognition or slight variations in illumination, this storage mechanism enables the system to retain the last known coordinates of the PV. As long as the PV's position does not change significantly, within a defined threshold $PV(x \pm 10, y \pm 10)$, the system maintains the stored coordinates as the PV presumed location, ensuring continuity in tracking and minimizing interruptions in power delivery. Only when the PV center position $PV(x', y')$ changes beyond the threshold due to actual

Optics EXPRESS

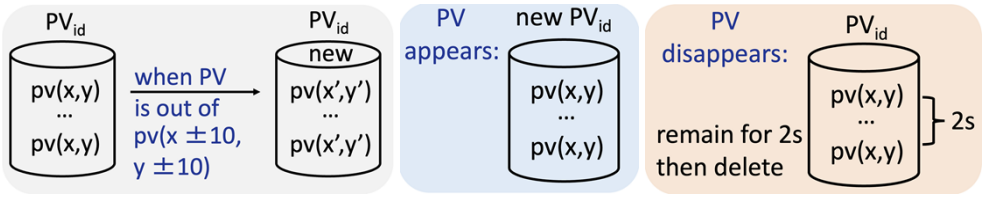

(a) (b) (c)

Fig. 11. (a) Data array storage for stabilizing PV center detection. (b) Stabilization of PV entering the 640×480 camera image. (c) Stabilization of PV leaving the camera image.

movement, the system updates the data array with the new coordinates. This mechanism thus filters out minor deviations in detection and focuses on meaningful position changes, reducing noise and maintaining stability in PV tracking.

As shown in Fig. 11(b) and (c), the system also includes mechanisms to manage PVs that either enter or leave the camera frame. For any newly detected PV in the frame, the system generates a new data array and assigns it a new PV_{id}, initializing it with the current PV center coordinates. This approach ensures that the system dynamically adapts to changes in the field of view, incorporating new PVs as they are detected.

For PVs that disappear from the frame, distinguishing between transient detection failures and actual exits from the field of view is essential. Temporary detection loss is managed by retaining stored coordinates until significant movement is detected. However, when a PV moves out of the frame entirely, the system incorporates a timeout mechanism. If a PV remains undetected for 2 seconds, the data array associated with its PV_{id} is removed, assuming it has permanently exited the frame. The 2 second threshold was determined experimentally to balance responsiveness and stability: a shorter duration risks misclassifying brief occlusions as exits, while a longer threshold delays the removal of obsolete data and degrades real-time performance. This delay accommodates brief detection losses and prevents premature deletion from the system's tracking memory.

The combination of data retention, threshold-based coordinate updates, and timeout-based array deletion mitigates the impact of detection fluctuations, ensuring a stable power supply to multiple PV targets. Furthermore, the stabilized detection of PV centers enhances the overall robustness of the system, particularly in wireless power transfer applications operating under varying ambient lighting conditions.

4. Setup and evaluation

4.1. Experiment setup

Based on the system design concept and optical simulation configuration, we established the experimental setup, as illustrated in Fig. 12. For the optical source, based on previous research on optimal candidates, we select an LED (OSRAM SFH4715AS; $\pm 60°$ divergence angle, 850 ± 10 nm wavelength) as the transmitter attached on an aluminum heatsink. This LED chip has a high-power density with 1.53 W radiant flux and 1×1 mm^2 chip size. A Fresnel lens (NTKJ, CF100) was used as the primary imaging element due to its large aperture, compact size, and lightweight characteristics. Additionally, to enable adaptive control of the spot size, a liquid lens (Optotune, EL-16-40-TC) was integrated into the system. This component allows for dynamic focus adjustment, enabling real-time fine-tuning of the IR beam's focal point.

The beam alignment and targeting mechanism is realized through a dual axis rotational system actuated by two series connected stepper motors, with a high torque motor (Nema 34) at the base and a lower torque motor (Nema 17) mounted above. The system is driven by Arduino via stepper

Optics EXPRESS

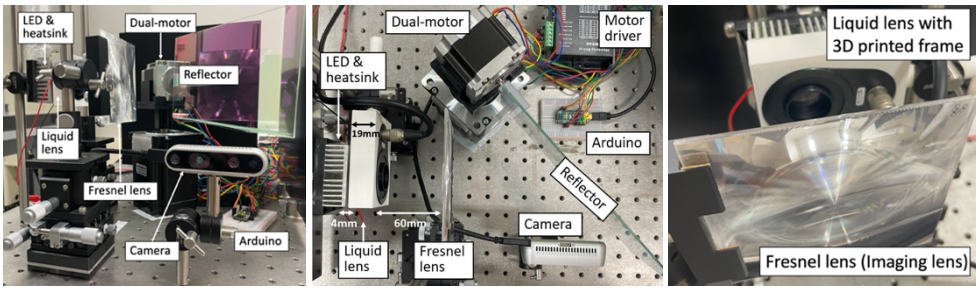

(a) (b) (c)

Fig. 12. Setup: (a) front view, (b) top view; (c) Liquid lens based adaptive lens system.

motor drivers (DM542), which achieves a resolution of 0.018° per step and a rotation speed of 15 RPM, ensuring an optimal balance between angular precision and mechanical stability. To enhance the efficiency of beam reflection, a custom-fabricated, high-reflectivity retroreflector (N706H0901) with dimensions of $110 \times 200\,\text{mm}^2$ is utilized. For the near-infrared wavelength range (LED spectrum $850 \pm 10\,\text{nm}$), this reflector achieves a reflectivity of 99% across an angular of 30° to 60°.

The experimental evaluation employs PV receivers of various sizes to validate the system's adaptability to different receiver geometries. Table 1 shows the three types of silicon-based PV cells with varying dimensions and the corresponding maximum output for 1-sun sunlight. Each PV bordered with a thin prism-type retroreflective sheet (TRUSCO HS-2222PW, 900 cd/lx/m^2), as shown in Fig. 13. This retroreflective configuration ensures the feasibility of IR-based PV detection under the dark environments. Additionally, a red LED indicator is integrated into the system to display the power supply status in real time. To assess the system's multi-receiver capabilities, five Si PV cells are randomly positioned at distances ranging from 2 m to 4 m. The auto-aiming and adaptive control system is designed with universality, which is compatible with any OWPT power source or specific application requirements.

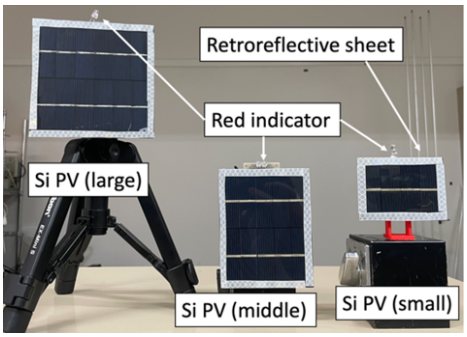

Fig. 13. The setup of multiple Si PV receivers with three different sizes.

4.2. Evaluation of detection and operation in varying lighting conditions

Accurate detection of the irradiation spot is essential for achieving effective power transfer in OWPT systems, especially when targeting small size PV cells positioned at varying distances. Figure 14 shows a comparative analysis between the conventional SSD-based detection method and the proposed optimized approach for localizing irradiation spots on PV surfaces.

Optics EXPRESS

Table 1. Parameters of three different size Si PV.

	large	middle	small
Effective size (mm^2)	102×102	75×102	45×65
Max. output (W)	2	1.15	0.5
Max. voltage (V)	6	5	2
Max. current (mA)	333	230	250

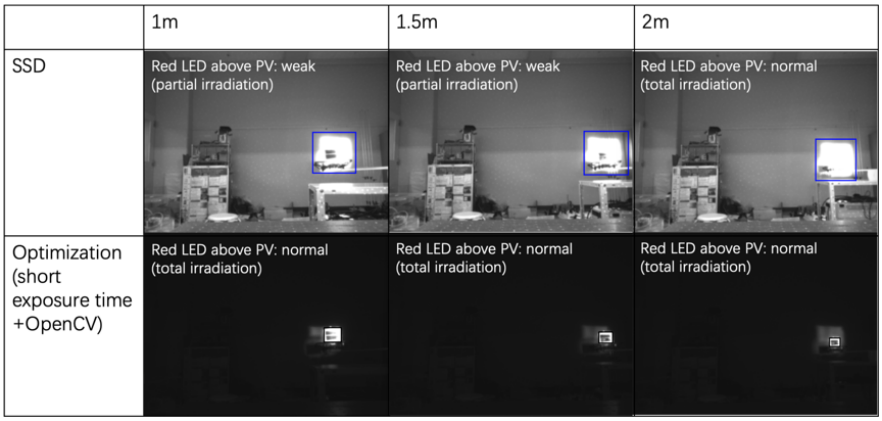

Fig. 14. Result of optimized spot detection algorithm. Comparison between the former CNN-based spot detection method and the proposed approach.

The CNN-based method exhibits limitations in detecting irradiation spots on smaller PV cells, particularly at shorter distances. It tends to detect large and diffused irradiation spots projected onto the background rather than accurately localizing the spot incident directly on the PV surface. Consequently, the system mistakenly aligns the PV module with the center of the luminous background spot instead of the true irradiation focus along the optical axis. This misalignment results in suboptimal energy transfer, with a part of the beam energy missing the PV cell. The inefficiency is evidenced by the weak illumination of the red indicator powered by the PV cells placed at 1~1.5 m, indicating insufficient PV output by inaccurate spot targeting.

In contrast, the optimized detection approach utilizes short-exposure imaging in conjunction with OpenCV-based image processing techniques to accurately segment the actual irradiation region on the PV surface, thereby improving detection precision. Across all tested distances from 1 m to 5 m, the optimized method consistently identifies a well-defined irradiation spot confined to the PV surface, free from background interference or spurious reflections. Furthermore, the integration of IR-based image processing allows for refined segmentation of the spot area, ensuring spatial correspondence with the true dimensions of the PV cell. This capability enables the system to reliably distinguish the PV module from surrounding structures, thereby facilitating accurate alignment and efficient power transmission.

Regarding the system's real-time tracking performance under varying illumination conditions, Fig. 15 and Visualization 1 illustrate the automated aiming and power delivery capabilities in both bright and dark modes with multiple PV receivers.

The system sequentially scans the PV modules from left to right, charging each receiver for 5s. In addition, the system continuously calculates the pixel value of the detected PV side length, and the longer side is recorded to control the beam spot size accordingly. The illumination level in a brightly lit environment provided by one fluorescent lamp, is approximately 500 lux, while in the absence of ambient lighting, the illumination approaches 0 lux. The results demonstrate that the

Optics EXPRESS

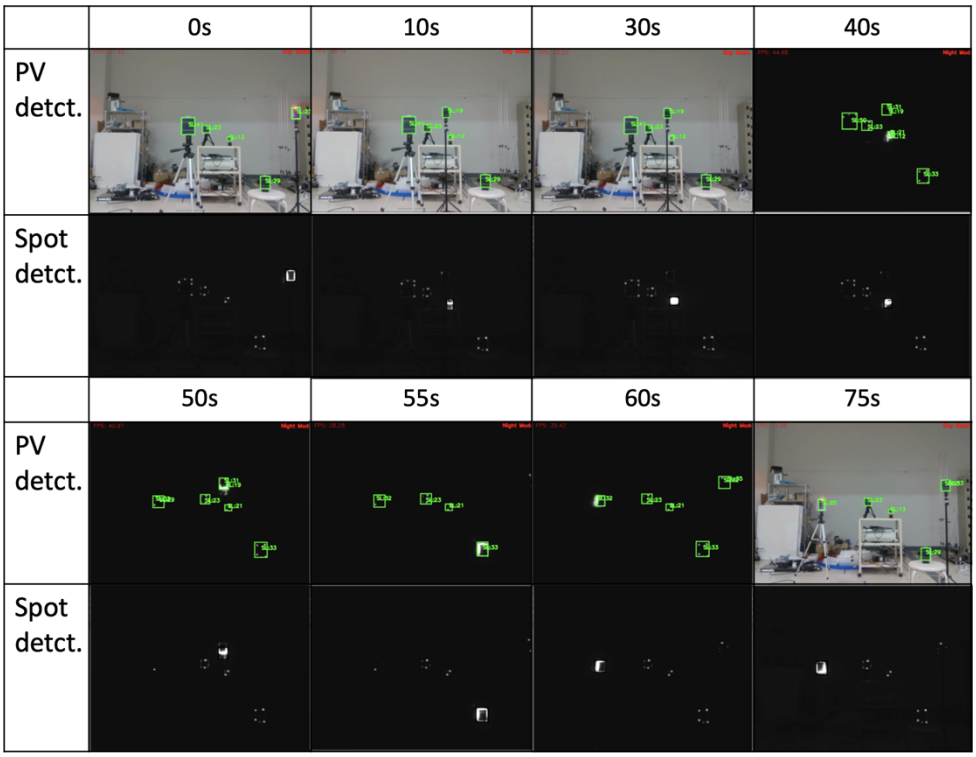

Fig. 15. Demonstration of automatic and adaptive OWPT for multiple PVs. PVs were moved and the sequences were changed during 0~10s and 50~60s. Pixel value of the detected PV's longer side length (SL) was displayed as "SL: value". This data was used to control the irradiation spot size, ensuring it remains consistent with the PV dimensions (Visualization 1).

switching latency between "day mode" and "night mode" is less than 50 ms in response to ambient light changes. This rapid adaptation allows for seamless real-time tracking and uninterrupted power delivery, even under dark conditions where receiver positions are varied. Furthermore, the system maintains high accuracy and reliability in detecting and targeting each PV receiver in sequence, confirming its effectiveness for scenarios that involve dynamic tracking across multiple receivers. For example, a PV moved out of the detection range in dark environment during 50~55s, yet the system continued to operate stably. The entire image processing pipeline is optimized to operate at over 30 frames per second (FPS), ensuring minimal latency and real-time responsiveness.

Furthermore, the detection range of the OWPT system is influenced by ambient lighting conditions. Under illuminated environments (illumination > 50 lux), the system employs RGB imaging for PV cell detection. In such conditions, both large and medium-sized PV cells can be reliably detected at distances of up to 5 m. However, for small PV cells, the effective detection range is reduced to approximately 3.5 m. This limitation is primarily due to their reduced pixel representation, typically fewer than 80 pixels in a 640×480 resolution image at greater distances, which compromises the detection accuracy of the SSD-based neural network in identifying these smaller targets.

In contrast, under low-light or unlit conditions, the system transitions to IR imaging, utilizing a combination of retroreflective materials and IR dot projection from a depth camera. Owing to the principle of retroreflection, the projected IR dots are reflected directly back toward the image

Optics EXPRESS

sensor, however, at extended distances, the IR dots become more dispersed, reducing their spatial density on the retroreflective surface. For small PV cells, this diminished dot density may lead to an insufficient IR signal being reflected, thereby preventing reliable detection. As a result, the effective detection range in night mode is approximately 4 m for the small size PV. In practical terms, these distances correspond to the maximum range at which a small receiver, such as half the size of a smartphone, can be reliably tracked and charged. It outlines the upper operational limits for IoT devices in typical indoor environments.

Note that day mode cannot be applied in unlit conditions because it captures visible light. On the other hand, night mode can be used in bright environments under the limited exposure conditions. However, as explained in above, a dual-mode approach combining both day and night modes can enhance recognition accuracy. This improvement is attributed to the system's ability to adapt to varying lighting conditions, target distances, and target sizes.

4.3. Evaluation of adaptive OWPT power supply performance

In the evaluation of the automated and adaptive OWPT system, two key performance metrics were analyzed, including power transmission efficiency, as well as adaptability across varying PV cell sizes and distances.

As for the power transmission efficiency, experimental results indicate that the lens system achieves an efficiency of approximately 56.2%. A detailed analysis of this performance is provided in the next section. Despite this limitation, the system's adaptive lens mechanism compensates by dynamically adjusting the focal length to maintain a consistent and optimized irradiation spot size at varying PV distances.

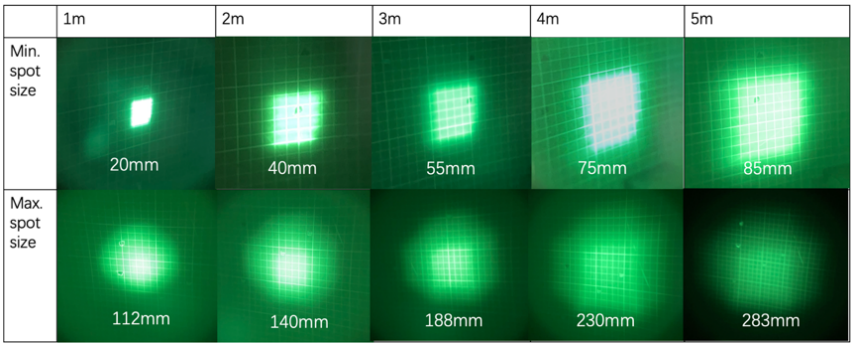

Fig. 16. Irradiation spot side length range at different distance.

As for the adaptive spot size control, Fig. 16 shows the irradiation spot dimensions at multiple distances, demonstrating the system's capability to modulate the spot size through the tunable focal length of the liquid lens. By adjusting the focus, the system can tailor the spot size to match the PV cell dimensions, ranging from a tightly concentrated spot for maximizing energy density on smaller cells to a broader beam suitable for larger targets. This functionality is particularly advantageous for medium and large PV cells, enabling stable and efficient power delivery at distances of up to 5 m. The effectiveness of this adaptability is further corroborated by the results shown in Fig. 17, where the system consistently maintains stable open-circuit voltages across PV cells of different sizes and at various distances, underscoring the robustness of the adaptive focusing approach.

Optics EXPRESS

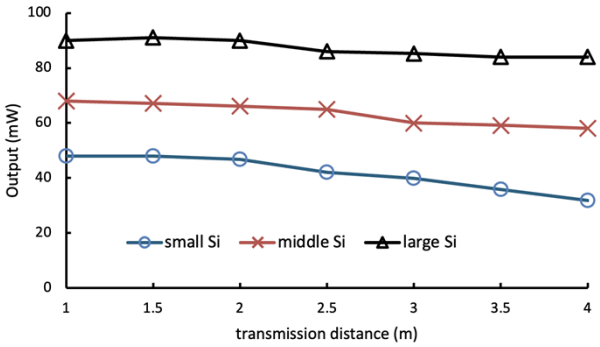

Fig. 17. Experiment outputs from 3 different size Si.

5. Discussion

In this study, we explored the OWPT with the ability to adjust the spot size based on the receiver's size, in order to improve the long-distance transmission performance. Despite these advantages, the lens system efficiency still exhibited 56.2% in the experiment. A detailed loss analysis reveals that two dominant factors contribute to this reduction.

First, approximately 30% of the loss is attributed to the limited aperture of the liquid lens, which has a diameter of only 16 mm and is positioned 15 mm from the light source. Due to the large LED divergence of ±60°, a portion of the emitted beam falls outside the lens aperture and is therefore not collected into the transmission path, leading to a large reduction in overall transmission efficiency.

Second, approximately 10% of the loss originates from the intrinsic optical properties of the liquid lens. The measured transparency of the lens at 850 nm is 89%. The lens comprises a double-layer glass structure enclosing optical fluid and an organic membrane. While the glass surfaces are anti-reflection coated at 850 nm, the organic membrane remains uncoated, resulting in additional Fresnel reflections. Furthermore, the optical fluid exhibits absorption in the near-infrared region, partially converting incident optical power into heat, so that a fraction of the incident power is dissipated within the lens itself.

This absorption also causes another practical challenge, a temperature-induced focal drift of the liquid lens. As the IR LED power source operates over time, it generates heat, raising the temperature of the lens and causing its focal length to shift. This thermal increase causes the optical fluid to expand, changing the lens shape and shifting its focal length. In our tests, the temperature rose from 24°C room temperature to around 38.9°C after 30 minutes, as shown in Fig. 18. Since the relationship between the focal length and spot size was determined in pre-experiments, any temperature-induced drift leads to a non-optimal spot size at its corresponding focal length, impacting the precision of spot control. A 10°C temperature change resulted in a shift of approximately 6 mm in the spot size.

To mitigate these limitations, further studies will focus on two strategies. First, the use of LEDs with smaller divergence or the integration of microlens directly on the LED chip can reduce beam truncation and improve collection efficiency. Second, we will investigate the relationship between temperature and focal length drift of the liquid lens, enabling feedback-based high-precision spot control to maintain stable transmission performance. With these improvements, the efficiency of the lens system is expected to exceed 80%, underscoring the promising potential of OWPT as a scalable solution for powering emerging IoT applications.

Optics EXPRESS

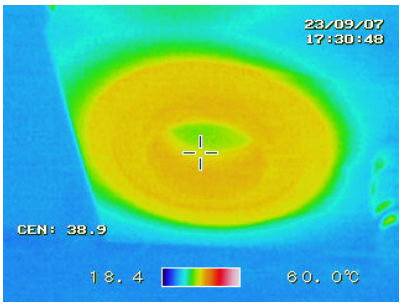

Fig. 18. Increased temperature at liquid lens surface causes the focal length drift.

6. Conclusion

This research presents the design and experimental validation of an automated and adaptive OWPT system capable of efficient and reliable power delivery. By integrating a liquid lens with dynamically tunable focal length, the system can precisely adjust the IR beam spot size in real time, enabling accurate targeting across PV receivers of varying sizes and distances, supporting effective power transmission up to 5 m.

In addition, the system operates seamlessly under both illuminated and dark environments. An optimized spot detection method enhances the localization accuracy of small irradiation spots, segmenting only relevant areas are targeted for charging. Under unlit conditions, PV receivers equipped with retroreflectors enable reliable detection within a range of approximately 4 m. This supports robust aiming and power transfer to multiple receivers, and fast mode switching without interruption. Experimental results demonstrate that the system maintains stable open-circuit voltages across different PV sizes and distances, confirming its adaptability and performance consistency. Overall, the proposed system offers a stable and versatile solution for wireless power transmission, with strong potential for deployment in daily or low-visibility environments.

Funding. Japan Science and Technology Agency (JPMJSP2106, JPMJSP2180); Tsurugi-Photonics Foundation (No. 20220502); Takahashi Industrial and Economic Research Foundation (No. I2-003-13).

Disclosures. The authors declare no conflicts of interest.

Data availability. Data underlying the results presented in this paper are not publicly available at this time but may be obtained from the authors upon reasonable request.

References

1. M. Molefi, E. D. Markus, and A. Abu-Mahfouz, "Wireless power transfer for IoT devices - a review," in *International Multidisciplinary Information Technology and Engineering Conference (IMITEC)* (2019), pp. 1–8.
2. M. Z. Chaari and S. Al-maadeed, "Wireless power transmission for the Internet of Things (IoT)," in *IEEE International Conference on Informatics, IoT, and Enabling Technologies (ICIoT)* (2020), pp. 549–554.
3. K. R. Li, K. Y. See, W. J. Koh, *et al.*, "Design of 2.45 GHz microwave wireless power transfer system for battery charging applications," in *Progress in Electromagnetics Research Symposium - Fall (PIERS - FALL)* (2017), pp. 2417–2423.
4. N. Shinohara, "The wireless power transmission: inductive coupling, radio wave, and resonance coupling," WIREs Energy and Environment **1**(3), 337–346 (2012).
5. C. Wu, H. Kim, S. Penugonda, *et al.*, "Analysis and modeling of the common-mode conducted EMI from a wireless power transfer system for mobile applications," IEEE Trans. Electromagn. Compat. **63**(6), 2143–2150 (2021).
6. T. Miyamoto, "Optical wireless power transmission using VCSELs," in *Semiconductor Lasers and Laser Dynamics VIII* (SPIE, 2018), 10682, p. 1068204.
7. A. W. Setiawan Putra, M. Tanizawa, and T. Maruyama, "Optical wireless power transmission using Si photovoltaic through air, water, and skin," IEEE Photonics Technol. Lett. **31**(2), 157–160 (2019).
8. O. Alamu, T. O. Olwal, and K. Djouani, "Simultaneous lightwave information and power transfer in optical wireless communication networks: An overview and outlook," Optik **266**, 169590 (2022).
9. T. D. P. Perera, D. N. K. Jayakody, S. K. Sharma, *et al.*, "Simultaneous wireless information and power transfer (SWIPT): recent advances and future challenges," IEEE Commun. Surv. Tutorials **20**(1), 264–302 (2018).

Optics EXPRESS

10. T. Miyamoto, "Optical wireless power transmission," in *Handbook of Radio and Optical Networks Convergence* (Springer, 2024), pp. 1093–1120.
11. J. Fakidis, S. Videv, S. Kucera, *et al.*, "Indoor optical wireless power transfer to small cells at nighttime," J. Lightwave Technol. **34**(13), 3236–3258 (2016).
12. Q. Liu, M. Xiong, M. Liu, *et al.*, "Charging a smartphone over the air: the resonant beam charging method," IEEE Internet Things J. **9**(15), 13876–13885 (2022).
13. N. Javed, N. L. Nguyen, S. F. A. Naqvi, *et al.*, "Long-range wireless optical power transfer system using an EDFA," Opt. Express **30**(19), 33767–33779 (2022).
14. D. Heo, K. Yang, S. Choi, *et al.*, "Optical wireless power transfer network system for multiple AE sensors," in *2024 IEEE Wireless Power Technology Conference and Expo (WPTCE)* (2024), pp. 493–496.
15. J. Kang, L. Sun, Y. Zhou, *et al.*, "Enhancing alignment accuracy in laser wireless power transmission systems using integrated target detection and perturbation-observation method," Photonics **11**(11), 1094 (2024).
16. L. Sun, J. Kang, Y. Bai, *et al.*, "Design and efficiency optimization of distributed laser wireless power transmission systems through centralized scheduling and current regulation," Photonics **12**(1), 30 (2025).
17. M. Kawakami and T. Miyamoto, "Dynamic optical wireless power transmission infrastructure configuration for EVs," Energies **18**(9), 2264 (2025).
18. "IEC 60825:2025 SER," https://webstore.iec.ch/en/publication/62424.
19. Y. Zhou and T. Miyamoto, "200 mW-class LED-based optical wireless power transmission for compact IoT," Jpn. J. Appl. Phys. **58**(SJ), SJJC04 (2019).
20. M. Zhao and T. Miyamoto, "Efficient LED-array optical wireless power transmission system for portable power supply and its compact modularization," Photonics **10**(7), 824 (2023).
21. D. Barolet, C. J. Roberge, F. A. Auger, *et al.*, "Regulation of skin collagen metabolism in vitro using a pulsed 660 nm LED light source," J. Investig. Dermatol. **129**(12), 2751–2759 (2009).
22. M. Al-Rubaiai and X. Tan, "Design and development of an LED-based optical communication system with active alignment control," in *International Conference on Advanced Intelligent Mechatronics* (2016), pp. 160–165.
23. M. Buffolo, C. D. Santi, M. Meneghini, *et al.*, "Long-term degradation mechanisms of mid-power LEDs for lighting applications," Microelectron. Reliab. **55**(9-10), 1754–1758 (2015).
24. Y. Guo, K. Pan, G. Ren, *et al.*, "Research on LED temperature characteristic and thermal analysis at low temperatures," in *13th IEEE International Conference on Electronic Packaging Technology & High Density Packaging* (2012), pp. 1411–1415.
25. M. Zhao and T. Miyamoto, "Optimization for compact and high output LED-based optical wireless power transmission system," Photonics **9**(1), 14 (2021).
26. M. Zhao and T. Miyamoto, "LED-based optical wireless power transmission for automatic tracking and powering mobile object in real time," IEEE Access **13**, 33643–33654 (2025).
27. M. Zhao and T. Miyamoto, "LED-based optical wireless power transmission through deep learning-enabled infrared spot recognition," in *Light-Emitting Devices, Materials, and Applications XXVIII* (SPIE Photonics West 2024), 12906, pp. 133–139.
28. K. Moriyama, K. Asaba, and T. Miyamoto, "Beam shape control system with cylindrical lens optics for optical wireless power transmission," Energies **18**(9), 2310 (2025).
29. Y. Zhou and T. Miyamoto, "Tolerant distance and alignment deviation analysis of LED-based portable optical wireless power transmission system for compact IoT," IEEJ Trans. EIS **141**(12), 1274–1280 (2021).
30. W. Liu, D. Anguelov, D. Erhan, *et al.*, "SSD: single shot multibox detector," in *Computer Vision – ECCV 2016*, (Springer International Publishing, 2016), pp. 21–37.
31. J. Redmon, S. Divvala, R. Girshick, *et al.*, "You only look once: unified, real-time object detection," in *IEEE Conference on Computer Vision and Pattern Recognition (CVPR)* (2016), pp. 779–788.